Journal of Sustainability for Energy
https://www.acadlore.com/journals/JSE

Water Distribution Uniformity Analysis in Low-Pressure Irrigation Manifolds using Computational Fluid Dynamics

Leila Riahinezhad[1], Ahmad Nooraeen[2*], Melika Mohammadkhah[3]

[1] Department of Sustainability and Energy, Mammut Group Company, 1513737511 Tehran, Iran
[2] Faculty of Biomedical Engineering, Amirkabir University of Technology, 1149754413 Tehran, Iran
[3] Institute of Mechanics, Technische Universität Berlin, 10623 Berlin, Germany

* Correspondence: Ahmad Nooraeen (ahmad.nooraeen@gmail.com)

Received: 01-25-2025 **Revised:** 03-12-2025 **Accepted:** 03-20-2025

Citation: L. Riahinezhad, A. Nooraeen, and M. Mohammadkhah, "Water distribution uniformity analysis in low-pressure irrigation manifolds using Computational Fluid Dynamics," *J. Sustain. Energy*, vol. 4, no. 1, pp. 82–95, 2025. https://doi.org/10.56578/jse040105.

Abstract: Efficient water management in agriculture increasingly depends on the ability to deliver uniform irrigation while minimizing energy consumption. Low-pressure irrigation systems have emerged as a sustainable alternative to traditional high-pressure networks, offering significant potential for small-scale and greenhouse applications. This study investigates the hydraulic and energy performance of low-pressure irrigation manifolds through a combined Computational Fluid Dynamics (CFD) analysis and performance assessment framework. The computational model simulates steady-state, incompressible flow within manifolds of two diameters (12 mm and 25 mm) and two emitter configurations (6 and 12 outlets), under inlet pressures of 50 kPa and 100 kPa. Detailed flow fields were analyzed in terms of pressure distribution, velocity contours, helicity, and wall shear stress, while outlet pressures and mass flow rates were used to evaluate distribution uniformity (DU). Mesh independence tests ensured numerical reliability, and hydraulic performance was quantified using standard indices such as the Coefficient of Variation (CV) and Christiansen's uniformity coefficient (CU). The results demonstrate a consistent pressure and discharge decline from the inlet to the downstream outlets, with localized hotspots of velocity, shear, and rotational flow near emitter junctions. The manifolds with smaller diameters and higher inlet pressures led to greater non-uniformity (CV up to 14.8%, CU $\approx$ 87%), while the manifolds with larger diameters significantly improved uniformity (CV < 6%, CU > 95%) at lower inlet pressures. Energy analysis showed a strong link between hydraulic performance and pumping demand: designs with better uniformity required significantly less energy, with total pumping energy dropping from 4470 kWh in the least efficient case to just 1072 kWh in the optimal one. These findings highlight that manifold diameter, emitter spacing, and operating pressure are critical determinants of system efficiency. Optimized designs featuring larger diameters and moderate pressures offer a dual benefit of enhanced water-use efficiency and reduced energy consumption. The results provide actionable guidelines for the design of sustainable low-pressure irrigation systems, particularly in small-scale and greenhouse applications, where uniform distribution and energy savings are essential.

Keywords: Low-pressure irrigation manifolds; Computational Fluid Dynamics (CFD); Water distribution uniformity (DU); Hydraulic performance indices; Coefficient of Variation (CV); Christiansen's uniformity coefficient (CU); Energy efficiency in irrigation systems

1 Introduction

The intensifying global challenge of water scarcity necessitates a paradigm shift in water resource management, particularly within the agricultural sector, which accounts for the largest share of freshwater consumption [1]. Efficient irrigation is no longer a matter of maximizing yield but a crucial component of environmental sustainability and food security [2]. Among various irrigation technologies, low-pressure systems, such as drip and micro-sprinkler irrigation, have gained prominence, especially for small-scale, protected, and sustainable agricultural settings like greenhouses and domestic farming [3]. These systems inherently minimize losses due to evaporation and deep percolation. However, the true efficiency of any irrigation system hinges on its distribution uniformity (DU) [4]. Hydrodynamically, DU is a measure of how evenly water is applied across the entire field or growing area. A low

DU leads to a detrimental cycle: Some plants are under-irrigated, stressing the need to over-water other zones, which in turn causes water waste, energy loss for pumping, and nutrient runoff [5]. Achieving high DU requires meticulous design and operation, focusing primarily on the hydraulic performance of the main components, notably the manifold (or sub-main) and the lateral lines. The manifold, a simple yet critical closed conduit, is responsible for splitting the main flow into multiple parallel outlets [6]. Maintaining uniform pressure and flow rate across these outlets, particularly under the inherently unstable conditions of low-pressure operation driven by low-power pumps, is a complex mechanical and hydraulic engineering challenge [7]. This issue is exacerbated in small, often homemade setups where standard design principles might be compromised. Therefore, the foundational necessity of any sustainable irrigation strategy is a detailed, physics-based understanding of the flow behavior within these manifold systems.

The hydraulic performance of an irrigation manifold is governed by the intricate interplay of several mechanical and fluid dynamics principles [8]. As water flows through the manifold, the pressure head is constantly changing due to two primary, counteracting mechanisms: Frictional head loss and pressure recovery (or momentum change) [9]. Frictional losses, driven by the fluid's viscosity and the pipe wall roughness, are progressive, causing a cumulative pressure drop along the flow direction [10]. However, as flow exits through successive outlets, the main flow rate within the manifold decreases, leading to a corresponding reduction in flow velocity. This deceleration causes a localized pressure recovery due to the conversion of kinetic energy back into potential (pressure) energy, a phenomenon particularly pronounced near each side-port branching [11]. The non-uniformity of flow rate from each emitter is a direct function of the spatial variation in pressure head along the manifold pipe, typically described by the Christiansen uniformity coefficient (CU) [12]. In low-pressure systems, the magnitude of the operating pressure is small, making the relative impact of these head losses and recoveries significantly more critical than in high-pressure installations [13]. For instance, a small absolute pressure drop system represents a 10% variation, potentially leading to unacceptable flow non-uniformity. Mechanically, the manifold's material, the geometry of the branching (T-junctions), and the precision of emitter placement all contribute to the localized head losses [14]. A critical design variable is the ratio of the total cross-sectional area of the outlets to the cross-sectional area of the main manifold, as this ratio dictates the overall resistance and the intensity of the pressure recovery effect [15]. Thus, the engineering task is to precisely balance the head loss against the head recovery to achieve a minimal net pressure variation, which in turn ensures uniform volumetric flow to all emitters.

Traditional methods for analyzing manifold flow, relying on simplified one-dimensional (1D) analytical models (such as the Darcy-Weisbach or Hazen-Williams equations modified for lateral flow) or empirical testing, often fall short of capturing the true three-dimensional (3D) fluid dynamics within the system [16, 17]. These simplified models inherently neglect complex local phenomena, such as the formation of vortices, flow separation, and the significant turbulence at the manifold-emitter branch junctions, especially where velocity vectors change direction abruptly. This is precisely where Computational Fluid Dynamics (CFD) becomes indispensable [18]. CFD provides a robust numerical framework to solve the governing Navier-Stokes equations, allowing for the simulation of steady-state (or transient) fluid flow under realistic boundary conditions, offering a high-fidelity visualization and quantification of pressure and velocity fields [18]. By modeling the intricate geometry of the manifold and its outlets, CFD can accurately calculate the subtle pressure gradients and the resulting flow partitioning at each junction, directly predicting the system's DU [19]. Specifically, the use of different models and the specification of boundary conditions, such as the low inlet pressure from small pumps and the specific head-loss characteristics of the simulated drip emitters, allow for a near-real-world assessment of performance without the high cost and labor of extensive field trials. Furthermore, CFD-derived data can be directly integrated with economic performance metrics by linking non-uniformity losses to wasted water volume and the excess pumping energy required to compensate for poor distribution [20, 21].

This comprehensive approach, coupling detailed hydraulic-mechanical simulation with a cost-benefit analysis, transforms the design process from an empirical trial-and-error method into a predictive, science-based optimization strategy for sustainable water management.

This study addresses the critical need for an integrated hydraulic and economic assessment of low-pressure irrigation manifolds by leveraging steady-state CFD analysis to specifically investigate the flow DU in simple manifold geometries, which are typical of low-cost, sustainable agricultural setups (e.g., home and greenhouse systems). The core of the analysis focuses on quantifying the effects of various mechanical and operational parameters on the resulting pressure and flow rate uniformity. Importantly, this work conducts a direct, systematic comparison between two fundamental manifold configurations. The comparative analysis is rigorously performed by systematically varying three key parameters: (1) inlet pressure to replicate variations in pump output), (2) manifold pipe diameter to represent a mechanical design choice, and (3) the number of operating emitters along the line. This systematic variation is performed while maintaining a constant manifold length and fixed emitter discharge characteristics. The simulation results are subsequently utilized to calculate a performance index and a parallel metric, quantifying water and energy savings. The novelty of this work lies in the development and application of an efficiency-driven CFD

framework that directly couples the high-fidelity hydraulic performance of low-cost, real-world manifolds (including the simulation of emitter resistance) with a comprehensive economic assessment for small-size sustainable irrigation systems. By providing a validated, geometry-specific design space for optimal low-pressure manifold operation, this research offers a tangible, data-driven methodology for engineers and small-scale farmers to transition from inefficient, conventional designs to hydrodynamically-optimized, resource-saving systems, thereby making a direct contribution to resilient water management in hydraulic engineering.

2 Methods and Materials

This section presents the computational methodology used to analyse the hydraulic performance and DU of low-pressure irrigation manifolds. Steady-state, incompressible flow within various manifold geometries was simulated using CFD to resolve pressure and velocity fields, particularly at branching points where flow distribution is most affected. The process involved defining geometry and boundary conditions, selecting an appropriate model, performing a mesh independence study, and specifying the hydraulic and mechanical parameters relevant to performance evaluation.

2.1 Manifold and Emitter Geometry

The manifold is modeled as a straight cylindrical pipe with a fixed length of 2.0 m, equipped with multiple side outlets representing the emitters (Figure 1). Two manifold diameters (12 mm and 25 mm internal diameter) and two emitter configurations (6 and 12 outlets) were considered to assess the influence of pipe size and outlet spacing on hydraulic performance.

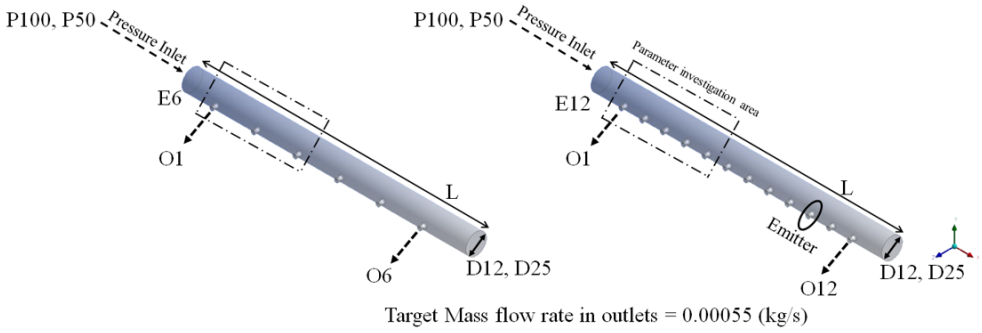

Figure 1. Geometry of the low-pressure irrigation manifold and applied boundary conditions, including inlet pressure, emitter outlets with specified mass flow rates, and no-slip wall conditions

2.2 Boundary Conditions

The simulations are defined by the following hydraulic boundary conditions. The working fluid is water at standard temperature, with a defined density ($\rho = 998.2\ \mathrm{kg/m^3}$) and dynamic viscosity ($\mu = 0.001003\ Pa.s$) [22]. A Pressure Inlet boundary condition is applied at the inlet of the manifold. Two scenarios are analyzed, representing typical low-power pump outputs: P100 which means 100 kPa and P50 means 50 kPa. A mass flow outlet boundary condition is applied to all emitter ports to simulate a specific target flow rate. The target mass flow rate [23] for each individual emitter is set to 0.00055 kg/s. This condition represents the design flow rate that an idealized system must achieve.

2.3 Governing Equations and CFD Setup

The flow of the water within the manifold is governed by the conservation laws of mass and momentum. Given the small pipe diameters typical of low-pressure irrigation, the flow is assumed to be incompressible, and in a steady-state condition. The governing equations, including the continuity equation and the Navier-Stokes momentum equations, are simplified for laminar flow given the low Reynolds numbers expected in these low-pressure systems. The Navier-Stokes equations for momentum conservation:

$$\nabla \cdot \overrightarrow{u_{\mathrm{w}}} = 0 \tag{1}$$

$$\rho\left(\frac{\partial\overrightarrow{u_{\mathrm{w}}}}{\partial t}+\overrightarrow{u_{\mathrm{w}}}\cdot\nabla\overrightarrow{u_{\mathrm{w}}}\right)=\nabla\tau \tag{2}$$

where, $\overrightarrow{u_{\mathrm{w}}}$ denotes the velocity vector of the water flow, ρ is the fluid density, and τ represents the shear stress tensor, which is defined as:

$$\tau=\mu\left(\nabla\overrightarrow{u_{\mathrm{w}}}+(\nabla u_{\mathrm{w}})^{\mathrm{T}}\right) \tag{3}$$

where, μ denotes the dynamic viscosity of the water, and the superscript T indicates the transpose operator.

2.4 Mesh Generation and Independence Study

The computational domain, encompassing the manifold and the emitter ports, is discretized using an unstructured, three-dimensional Tetrahedral Mesh. This element type is highly flexible and well-suited for capturing the geometric complexity of the T-junctions at the emitter outlets. Particular attention is given to generating a finer mesh resolution near the pipe walls and at the high-gradient regions, specifically the T-junctions, where flow separation and high shear rates are expected.

To ensure that the simulation results are independent of the grid resolution and accurately represent the underlying physics, a comprehensive mesh independence study is conducted. This involves performing simulations on a sequence of progressively finer meshes. The key parameter chosen for the convergence criterion is the wall shear stress (WSS), a critical mechanical indicator of frictional losses and momentum exchange, averaged over the manifold wall. The mesh size is considered converged when the relative difference in the WSS between the two successively refined meshes falls below a predetermined tolerance threshold. In this study, the target convergence is set such that the variation in WSS between the final two mesh resolutions is less than 3%. The final, selected mesh is the one corresponding to the finer of the two meshes meeting this criterion. This process confirms that numerical errors due to mesh discretization are minimized and the computed hydraulic parameters are reliable. Figure 2 illustrates the computational mesh generated for the manifold and emitter geometry.

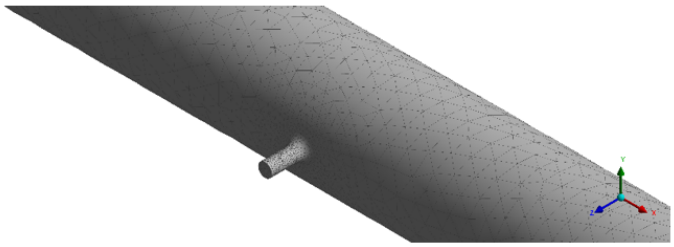

Figure 2. Tetrahedral mesh of the manifold and emitter geometry

2.5 Hydraulic and Mechanical Performance Metrics

The simulation outputs are processed to extract both fundamental fluid mechanics such as pressure and velocity data and key hydraulic performance indices necessary for a complete engineering assessment. Pressure contours in the longitudinal section and at the branching zones (as shown in Figure 1) are analyzed to visualize the pressure distribution and identify regions of significant head loss or recovery. Flow velocity magnitude are examined to understand the macroscopic flow pattern, identify recirculation zones at the T-junctions, and confirm the laminar nature of the flow. This metric is computed to quantify the degree of swirling motion or vorticity within the manifold, particularly at the branching junctions, as it directly relates to secondary flow losses and momentum change. WSS is quantified across the manifold walls to accurately determine the frictional head losses for each geometric configuration. Average pressure and mass flow rate are extracted for each of the individual emitter outlets and plotted against the emitter number to visually assess the uniformity.

The following parameters are calculated from the outlet flow rates. The average flow rate ($\bar{Q}$) per emitter and the total flow rate (Q_{total}) are determined and compared against the theoretical required total flow.

$$\bar{Q}=\frac{1}{\mathrm{N}}\sum_{1}^{\mathrm{N}}Q_i \tag{4}$$

$$Q_{\text{total}} = \sum_{1}^{N} Q_i \tag{5}$$

Q_i is the mass flow of emitter number i and N is the total number of emitters. Coefficient of Variation (CV) measures the precision of the manufacturing or uniformity of the emitters themselves:

$$Q^{\sigma} = \sqrt{\frac{\sum_{1}^{\mathrm{N}} \left(\bar{Q} - Q_i\right)^2}{\mathrm{N}}} \tag{6}$$

$$\mathrm{CV} = \frac{Q^{\sigma}}{\bar{Q}} \tag{7}$$

where Q^{σ} is the standard deviation of the flow rates.

CU is a measure of hydraulic uniformity based on the variability of the flow rates, often used in sprinkler and drip systems [6].

$$\mathrm{CU} = 100 - \frac{\sum_{1}^{\mathrm{N}} \left|\bar{Q} - Q_i\right|}{\mathrm{N}\bar{Q}} \tag{8}$$

The energy consumption is calculated using the required total head and the total discharge. The difference in pressure between the inlet and the outlet target pressure is used to estimate the work required by the pump, providing the foundation for the economic performance assessment and water/energy saving calculations.

3 Result

The numerical simulations provide both qualitative and quantitative insights into the flow distribution and the hydraulic behavior of the low-pressure irrigation manifolds under various geometric and operational conditions.

3.1 Pressure Contour

Figure 3 illustrates the pressure contours along the XZ plane of the irrigation manifold for two pipe diameters (D12 and D25), two emitter configurations (E12 and E6), and inlet pressures of 100 kPa (P100) and 50 kPa (P50). The maximum pressure, located at the near inlet cross-section, corresponds to the applied boundary condition in each case (approximately 100 kPa or 50 kPa gauge). The minimum pressure appears at the downstream end near the last emitter locations, approaching values close to 5,000 Pa depending on the configuration. Across all panels, the contours clearly reveal a gradual pressure decline from the inlet toward the end of the manifold, with the magnitude and spatial extent of the drop varying according to manifold diameter, emitter spacing, and inlet pressure.

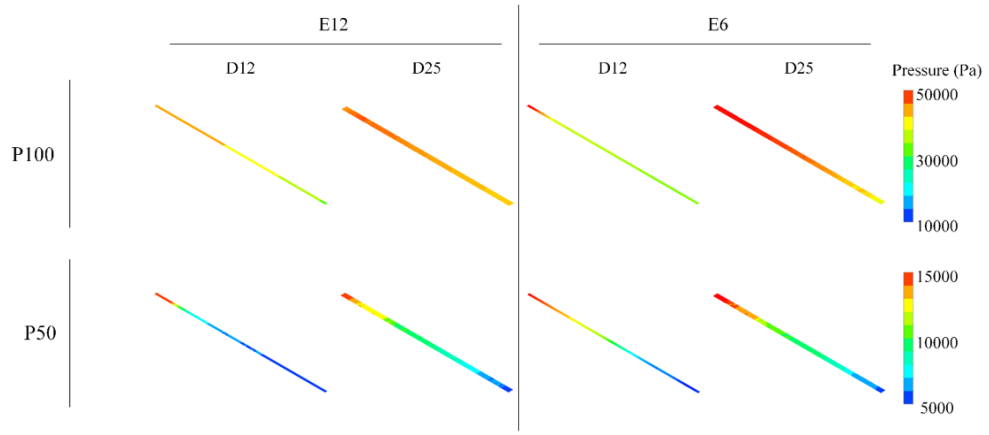

Figure 3. Pressure distribution on the XZ plane of the manifold. Maximum values occur near the inlet, while minimum pressures appear at the downstream emitters, showing a gradual decline along the manifold

3.2 Velocity Contour

Figure 4 illustrates the velocity distributions along the XZ plane of the irrigation manifold for two pipe diameters (D12 and D25), two emitter configurations (E12 and E6), and inlet pressures of 100 kPa (P100) and 50 kPa (P50). The maximum velocity is observed at the inlet cross-section and in the regions immediately adjacent to the first emitter junctions, with values reaching the 1.86 m/s. The minimum velocity occurs near the downstream end of the manifold and within recirculation zones at the emitter outlets. The magnified views highlight the detailed flow structures at the emitter junctions. In these regions, high velocity jets emerge from the main pipe toward the emitter ports, 1.5 m/s, while low velocity zones form immediately downstream of the junctions, indicated in green and blue. These enlarged sections also display the shear layers and velocity gradients around the T-junctions, which are particularly pronounced in the smaller diameter manifold (D12) and under higher inlet pressure (P100). Such localized flow features emphasize the complex hydrodynamic interactions at the emitter branches that influence overall DU.

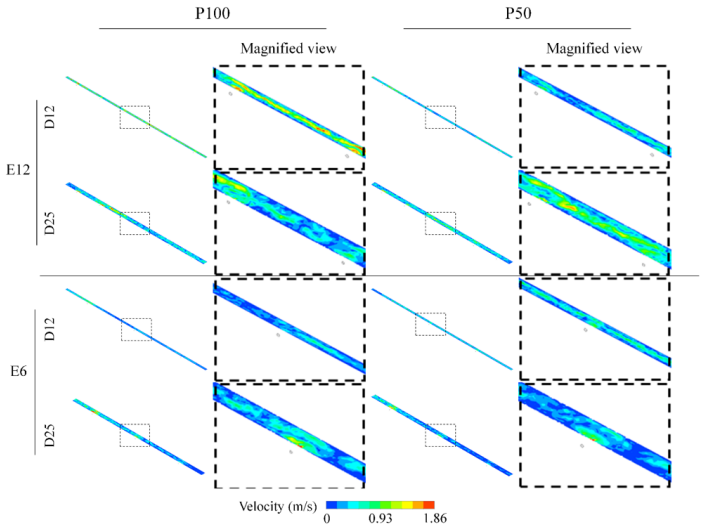

Figure 4. Velocity contours on the XZ plane of the manifold. High velocities are concentrated near the inlet and emitter junctions, whereas low velocities occur downstream. Magnified views reveal localized jets and recirculation zones at the side branches

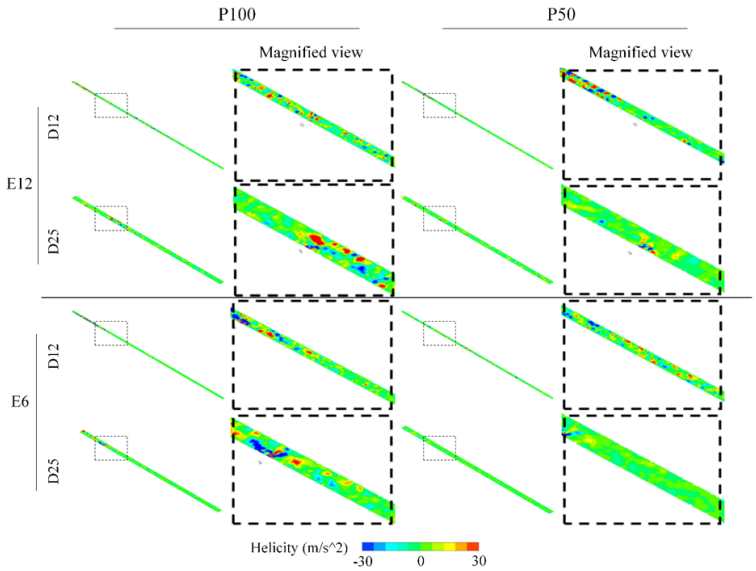

Figure 5. Helicity distribution on the XZ plane of the manifold. Positive (red) and negative (blue) helicity regions are concentrated around emitter junctions, while the main pipe flow remains largely axial. Magnified views emphasize rotational flow structures at the branch connections

3.3 Helicity Distribution

Figure 5 illustrates the helicity distribution along the XZ plane of the irrigation manifold for two pipe diameters (D12 and D25), two emitter configurations (E12 and E6), and inlet pressures of 100 kPa (P100) and 50 kPa (P50). The maximum helicity values occur at the emitter junctions where sharp velocity gradients and secondary flows are generated, whereas the minimum values are also localized around these branch connections but with opposite rotational direction. Along the main pipe axis, helicity values remain comparatively low, highlighted in green and light shades, indicating near-straight axial flow between emitters.

The magnified views provide a clearer visualization of the rotational flow structures near the emitter outlets. These enlarged regions reveal concentrated zones of both positive and negative helicity adjacent to the junction walls, reflecting localized swirling motion induced by the side-branch connections. The patterns are more distinct in the smaller diameter manifold (D12), under higher inlet pressure (P100), and near to the inlet, where stronger velocity gradients amplify the rotational effects. Across all scenarios, the contours demonstrate that helicity is predominantly a local phenomenon confined to the emitter junctions, while the bulk flow within the main manifold remains largely axial.

3.4 WSS Distribution

Figure 6 illustrates the WSS distribution along the inner surface of the irrigation manifold for two pipe diameters (D12 and D25), two emitter configurations (E12 and E6), and inlet pressures of 100 kPa (P100) and 50 kPa (P50). The maximum WSS ($\sim$ 9.64) is observed near the inlet region and around the first emitter junctions, where sharp velocity gradients occur due to sudden flow diversion. The minimum WSS (< 1 Pa) is recorded along the downstream wall segments, particularly close to the last emitters, where the velocity field is considerably reduced.

The magnified views focus on the emitter junctions and reveal localized zones of elevated shear stress. These regions appear with high WSS (> 6.2 Pa), concentrated at the junction walls and immediately upstream of the emitter outlets, reflecting the strong momentum exchange between the main pipe and side branches. In contrast, adjacent areas downstream of the emitters display extended regions of low WSS (< 2.2 Pa), indicating reduced wall friction in recirculation zones. The patterns are more pronounced for the smaller diameter manifold (D12) and under the higher inlet pressure (P100), where higher flow velocities intensify the wall shear.

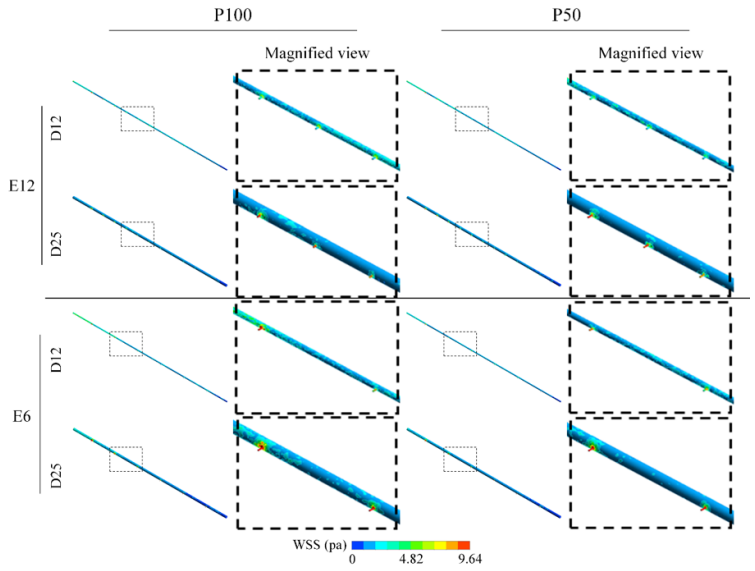

Figure 6. WSS contours along the manifold wall surface. Elevated WSS values are observed near the inlet and emitter junctions, while lower values dominate the downstream regions. Magnified views reveal localized shear zones at the side-branch connections, highlighting areas of intensified flow interaction

3.5 Outlet Average Pressure

Figure 7 presents the outlet average pressure values for the different manifold configurations, comparing two pipe diameters (D12 and D25), two emitter arrangements (E12 and E6), and two inlet pressures (P100 and P50). The data are shown as a series of plots where the pressure at each emitter outlet is displayed sequentially along the manifold length. In all cases, the maximum outlet pressure corresponds to the first emitters near the inlet, while the minimum values are associated with the last emitters at the downstream end. For P100, the initial outlet pressures

are close to 60,000 Pa, gradually decreasing along the distribution line, while for inlet pressure of 50 kPa (P50), the initial values start near 20,000 Pa and follow a similar downward trend. The curves allow a direct comparison between pipe diameters and emitter configurations. For D12, the pressure drop between the first and last emitters is more pronounced, while in D25, the reduction is less steep. Similarly, configurations with more emitters (E12) exhibit a denser set of pressure points along the length, whereas E6 shows fewer but more widely spaced data points, reflecting the larger spacing between outlets.

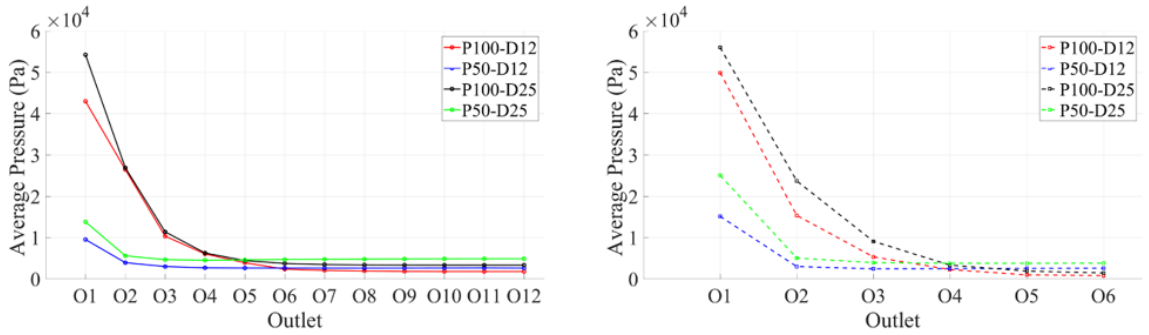

Figure 7. Outlet pressure distribution for each emitter along the manifold length. Results are compared for D12 and D25, E12 and E6 configurations, and two inlet pressures. The plots show higher pressures near the inlet emitters and progressive reductions toward the last outlets

3.6 Mass Flow Rate

Figure 8 presents the mass flow rates at the emitter outlets for two manifold diameters (D12 and D25), two emitter configurations (E12 and E6), and inlet pressures of 100 kPa (P100) and 50 kPa (P50). The results are plotted sequentially along the manifold length, with each point representing the discharge from an individual emitter. The maximum outlet flow rates are consistently recorded at the first emitters near the inlet, while the minimum flow rates appear at the downstream end, close to the last emitters. For the higher inlet pressure case (P100), the initial outlet flows reach values close to the design target of 0.00055 kg/s, while under reduced inlet pressure (P50), the discharge values are noticeably lower. The plots clearly show a gradual decline in outlet mass flow along the manifold length, reflecting the pressure losses observed in Figure 7. Comparing emitter configurations, both arrangement E6 and E 12 follow the same general downward trend.

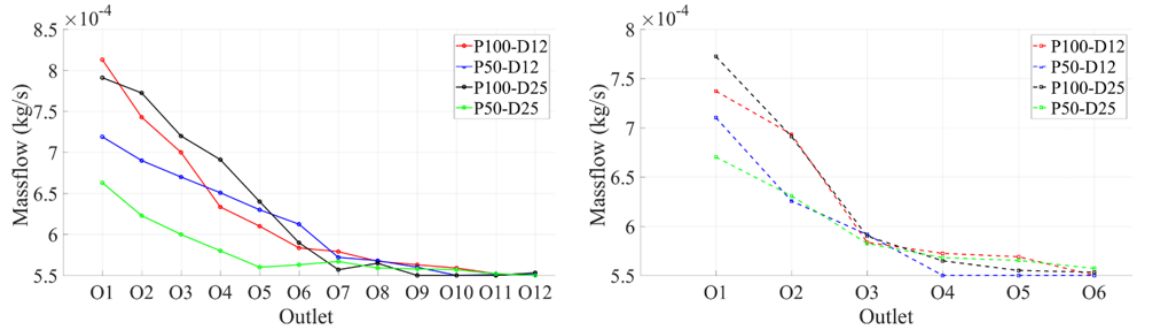

Figure 8. Mass flow rate at the emitter outlets. The discharge values are highest at the first emitters and gradually decrease downstream, reflecting the hydraulic losses along the manifold

3.7 Hydraulic Performance Metrics

Table 1 summarizes the hydraulic performance metrics obtained from the CFD simulations for the various manifold configurations. The results are reported for two pipe diameters (D12 and D25), two emitter arrangements (E12 and E6), and two inlet pressures (P100 and P50). The performance indicators include the CV, the Christiansen CU, the average and total outlet discharge, and the estimated pumping energy consumption. The CV ranges from a minimum of 5.96% (D25–E12 at P50) to a maximum of 14.76% (D12–E12 at P100). The corresponding CU

varies between 87.32% and 95.52%, with the highest values observed for the larger diameter pipe (D25) operating at lower inlet pressure (P50). The average discharge per emitter remains close to the design target of 0.00055 kg/s across all cases, with values between 0.000578 kg/s and 0.000627 kg/s. The total discharge depends on the number of emitters: For E12 configurations, it is approximately 0.0073–0.0075 kg/s, while for E6 configurations; it is nearly half, about 0.00357–0.00373 kg/s. The pumping energy consumption shows the largest variation among scenarios. For 12 emitters with a small pipe diameter at high inlet pressure (D12–E12 at P100), the energy demand reaches 4470.06 kWh, whereas for the six-emitter configuration with a larger diameter pipe at low inlet pressure (D25–E6 at P50), it decreases to only 1071.73 kWh.

Table 1. Hydraulic performance indicators for different manifold configurations. Reported parameters include the coefficient of variation, Christiansen's uniformity coefficient, average and total discharge, and estimated pumping energy consumption

Number of Emitters	**E12**				**E6**			
Diameter of Manifold	D12		D25		D12		D25	
Pressure Inlet	P100	P50	P100	P50	P100	P50	P100	P50
CV (%)	13.84	9.91	14.76	5.96	12.59	10.69	14.57	7.56
CU (%)	89.13	91.53	87.32	95.52	90.96	93.13	89.81	94.74
Q Average (kg/s)	0.000621	0.00061	0.000627	0.000578	0.000618	0.000596	0.000621	0.000596
Q Total (kg/s)	0.007453	0.007324	0.007529	0.006932	0.003706	0.003577	0.003727	0.003574
Energy consumption (kWh)	4470.06	2196.43	4515.88	2078.73	2222.47	1072.82	2235.01	1071.73

4 Discussion

As it is demonstrated in Figure 3, the axial decay of static pressure along a pressurized lateral or manifold is consistent with both experimental and numerical investigations of drip/lateral lines reported in the literature [24–26]. Previous studies have documented progressive pressure loss along lateral lines and manifolds driven by frictional head loss and successive emitter discharge [27]. CFD studies together with laboratory tests show that larger internal diameters reduce head loss per unit length and minimize pressure drop along the distribution line, resulting in better pressure retention at downstream outlets. This finding aligns with other numerical studies of manifold modeling that explicitly show reduced pressure gradients for larger channel diameters [13, 28, 29]. Several investigations likewise highlight the role of emitter count and spacing in determining the spatial pressure profile. For example, configurations with more closely spaced emitters (higher emitter density) produce a denser sequence of local pressure extractions along the manifold, yielding a steeper cumulative pressure decline compared with arrangements with fewer, more widely spaced outlets [30, 31]. This behavior is consistent with field and experimental reports that link lateral length and emitter spacing to non-uniformity in emission along the line [26]. At the same time, studies that employ pressure-compensating emitters or system-level pressure regulation have shown substantially improved outlet uniformity and greatly reduced sensitivity of downstream pressure to manifold geometry; in such cases, emitter/regulator behavior (rather than manifold diameter alone) governs the outlet pressure and flow uniformity. Differences between these reports and our findings can primarily be attributed to emitter type (compensating vs non-compensating), the inclusion of pressure regulators, and the scale/length of the lateral system studied [32].

The pattern of velocity and its peaks near the inlet and surrounding branching points is consistent with studies of manifold or lateral systems [33, 34]. For instance, in a study reported that flow acceleration tends to concentrate near manifold inlets and branching regions due to local constriction, while interior downstream segments exhibit lower velocities [33]. Similarly, another study on modeling of manifold uniformity showed that velocity magnitudes progressively decrease along the manifold as pressure losses accumulate [34]. However, some studies report contrasting results, especially in systems with alternative manifold geometries or special flow-control elements. For example, in a CFD study of a modular manifold [35], velocity variations were tempered by internal channel design modifications, such that lateral flow acceleration zones were less abrupt, and the velocity field appeared more homogenized. The discrepancy arises mainly because their manifold design included internal features (e.g. flow guides or staged divisions), which act to smooth out local velocity peaks and promote more uniform velocity distribution across branches.

The presence of nonzero helicity in the vicinity of emitter junctions is consistent with classical fluid dynamics understanding. Helicity quantifies the alignment between velocity and vorticity fields, so regions where the flow

diverges into branches naturally generate swirl or secondary rotational behavior. Indeed, a foundational review states that helicity measures the linkage or twisting of vortex lines in a flow and is an important diagnostic of three-dimensional flow complexity (especially in branching or curved geometries) [36]. Therefore, our results are broadly in line with theoretical expectations of helicity concentration in zones of strong shear or geometric perturbation. Comparisons with numerical and experimental studies that explicitly report helicity in branched flow systems are limited, but a few analogies can be drawn. For instance, in three-dimensional cavity or swirling flows, helicity is often found concentrated around separation vortices and geometric discontinuities where local rotational structures are pronounced [37]. In those contexts, regions of high helicity often mirror zones of strong vorticity-velocity interaction, which is qualitatively similar to what is observed near emitter junctions. Some investigations in internal manifold flows assume quasi-two-dimensional or axisymmetric approximations that effectively suppress swirl, thus yielding negligible helicity fields; under such assumptions, helicity may appear uniformly near zero, in contrast to our distinct positive/negative patches. The discrepancy arises because such models neglect 3D branching effects or simplify junction geometry to eliminate swirl, whereas our full 3D CFD resolves these local rotational structures [38].

The high WSS near entry and branch junctions and lower WSS at downstream walls observed in Figure 6 align with the general principles of boundary layer theory and prior CFD studies of branched internal flows. When fluid encounters a sudden change in direction of flow (as at a T-junction), velocity gradients in the boundary layer intensify, producing elevated shear stress on the wall. Several manifold or microchannel CFD works report similar phenomena, where junctions or sharp bends concentrate WSS and downstream regions are relatively quiescent [39]. However, some studies report more uniform WSS distributions, particularly when employing smoothing features or rounded transitions. For example, works on optimized manifold designs or flow-guiding inserts show that local shear peaks can be alleviated by introducing fillets or rounded branch entrances, thereby moderating WSS gradients. The divergence from our sharp-junction geometry stems from these design differences: Smoother transitions reduce abrupt velocity gradients and thus dampen shear stress peaks.

This pattern of pressure outlet and mass flow rates are consistent with numerous experimental and numerical studies of drip irrigation laterals and manifolds, which have long reported that pressure declines progressively along the pipe due to frictional losses and extraction through outlets [34, 40–42]. Similar results are also found in another study, who observed steeper pressure decay in smaller diameter manifolds [29].

The CV values in this study range from 5.96% (D25–E12 at P50) to 14.76% (D12–E12 at P100). Lower CV indicates more consistent outlet discharge and, consequently, reduced water wastage. In practical irrigation terms, configurations with lower CV deliver closer-to-uniform water application, meaning less over- or under-irrigation at specific plants. The CU values, varying between 87.32% and 95.52%, confirm that all tested cases perform within the acceptable range for irrigation systems (CU > 85%), with larger diameters (D25) and lower inlet pressure (P50) achieving the best uniformity. These results are consistent with earlier reports showing that larger pipe diameters and moderate inlet pressures improve DU [26, 33].

Linking these indices to water saving potential, configurations with high CU and low CV inherently promote water-use efficiency. In such cases, more of the supplied water is evenly distributed and less is lost to spatial variability. Conversely, when CV is high (> 12%), some outlets over-discharge while others under-supply, forcing farmers to apply excess water to meet crop requirements at the driest points, effectively reducing irrigation efficiency. Thus, D25 at P50 demonstrates the most water-efficient performance, while D12 at P100 is the least favorable in terms of uniformity-driven efficiency.

The pumping energy consumption ranges widely, from 1071.73 kWh (D25–E6 at P50) up to 4470.06 kWh (D12–E12 at P100). Interestingly, the scenarios with the lowest CV and highest CU, particularly D25 under P50, also correspond to the lowest energy consumption. This correlation suggests that improved uniformity does not require additional energy cost; instead, optimized geometries simultaneously reduce hydraulic losses and pumping demand. In contrast, the smallest diameter at high pressure (D12–E12, P100) yields both the poorest uniformity and the highest energy expenditure, underscoring its inefficiency.

These findings align with several studies that link hydraulic uniformity to reduced energy consumption. Some have shown that designs with smoother pressure gradients not only enhance the coefficient of uniformity (CU) but also reduce head loss, thereby lowering pump power requirements [29, 34]. In contrast, studies examining pressure-compensating emitters report that CU can be maintained even at higher energy inputs, as internal regulation mechanisms ensure outlet uniformity [32]. This contrast stems from the type of emitters used: Our system assumes non-compensating outlets, where geometry and operating pressure play the dominant role. In compensated systems, by contrast, uniformity is maintained through emitter mechanics, shifting the performance burden away from pump efficiency.

The findings highlight that manifold diameter, emitter spacing, and inlet pressure are key geometric and operational factors governing pressure and discharge uniformity in non-compensating systems. Localized hotspots of velocity, helicity, and WSS occur primarily at emitter junctions, which can intensify non-uniformities and mechanical wear, especially in smaller-diameter pipes or under high inlet pressures. Practical design strategies such as smoothing

branch geometry, moderating inlet velocity, or adopting variable cross-sections can mitigate these effects. Moreover, incorporating pressure-compensating emitters or regulators fundamentally alters the relationship between geometry and performance, emphasizing the importance of emitter type in system design. Finally, configurations with larger diameters and moderate pressures not only improve hydraulic uniformity (low CV, high CU) but also reduce pumping energy demand, offering an optimal balance of water-use efficiency and sustainability for greenhouse and small-scale irrigation applications.

This study is subject to several limitations that should be acknowledged. The simulations were conducted under steady-state and laminar flow assumptions, neglecting potential transient effects, turbulence, and variability in real field conditions such as clogging or emitter manufacturing defects. The emitter outlets were modeled as idealized openings with prescribed discharge, while in practice, emitter performance is influenced by pressure-compensating mechanisms, clogging resistance, and material aging. Additionally, the manifolds considered here were of fixed length and uniform diameter, without exploring tapered or variable cross-sectional designs that may further improve hydraulic uniformity. Future research could address these limitations by incorporating transient flow simulations, testing with non-Newtonian or sediment-laden water, and coupling CFD with experimental validation in laboratory and field settings. Moreover, extending the analysis to smart irrigation technologies, including adaptive pressure regulation and sensor-controlled manifolds, would provide valuable insights for developing more resilient and energy-efficient irrigation systems.

5 Conclusion

This study employed steady-state CFD simulations in combination with hydraulic and economic performance metrics to assess the flow behavior and DU of low-pressure irrigation manifolds. The results demonstrated that:

• Manifold internal diameter, emitter spacing, and inlet pressure are critical design parameters governing pressure decay, velocity distribution, helicity formation, and WSS along the manifold.

• Pressure and velocity fields revealed a consistent decline from inlet to outlet, with localized hotspots of shear and rotational flow occurring at emitter junctions.

• Smaller-diameter manifolds and higher inlet pressures intensified these gradients, leading to greater non-uniformity and higher energy requirements. In contrast, larger-diameter manifolds operating under moderate inlet pressures achieved superior hydraulic uniformity, with lower CV (CV < 6%) and higher Christiansen's CU (CU > 95%), while simultaneously reducing pumping energy consumption by more than half compared with less efficient configurations.

From a design perspective, these findings highlight that optimizing manifold geometry can simultaneously enhance irrigation efficiency and reduce operational costs. Recommended strategies include increasing pipe diameter, smoothing branch junctions, or moderating inlet pressure that can mitigate flow non-uniformities and mechanical stresses, while the adoption of pressure-compensating emitters or regulators can further stabilize discharge irrespective of manifold geometry. The combined analysis of hydraulic indices and energy consumption confirms that designs featuring larger diameters and moderate pressures represent the most sustainable and cost-effective choice for small-scale agricultural and greenhouse irrigation systems.

This study offers a comprehensive CFD-based framework for evaluating the performance of low-pressure irrigation manifolds, effectively bridging detailed fluid mechanics with practical design guidance. By combining hydraulic analysis with energy consumption metrics, it reinforces established hydraulic principles while also delivering actionable insights for engineers, designers, and practitioners. The findings support more sustainable irrigation system designs by demonstrating how relatively simple design adjustments such as optimizing pipe diameter and inlet pressure can lead to significant improvements in water-use efficiency and reductions in energy demand. These insights are particularly valuable for small-scale agricultural and greenhouse systems (low-pressure irrigation networks), where cost-effective and energy-efficient solutions are critical for long-term sustainability.

Author Contributions

Conceptualization, L.R. and A.N.; Methodology, A.N. and M.M.; Software, L.R. and A.N.; Validation, A.N. and M.M.; Formal analysis, A.N.; Data curation, L.R.; Writing-original draft preparation, A.N. and M.M.; Writing-review and editing, A.N.and M.M.; Visualization, L.R. All authors have read and agreed to the published version of the manuscript.

Data Availability

The data used to support the research findings are available from the corresponding author upon request.

Conflicts of Interest

The authors declare no conflict of interest.

References

[1] K. Javan, A. Altaee, S. BaniHashemi, M. Darestani, J. Zhou, and G. Pignatta, "A review of interconnected challenges in the water-energy-food nexus: Urban pollution perspective towards sustainable development," *Sci. Total Environ.*, vol. 912, p. 169319, 2024. https://doi.org/10.1016/j.scitotenv.2023.169319

[2] C. Taguta, T. L. Dirwai, A. Senzanje, A. Sikka, and T. Mabhaudhi, "Sustainable irrigation technologies: A water-energy-food (WEF) nexus perspective towards achieving more crop per drop per joule per hectare," *Environ. Res. Lett.*, vol. 17, no. 7, 2022. https://doi.org/10.1088/1748-9326/ac7b39

[3] M. Buhshan, P. Kumar, and B. B. Sahoo, "Advancements in precision irrigation techniques for sustainable water management," in *Farming for the Future: Smart Agriculture Innovations*, 2023, pp. 43–60.

[4] L. Levidow, D. Zaccaria, R. Maia, E. Vivas, M. Todorovic, and A. Scardigno, "Improving water-efficient irrigation: Prospects and difficulties of innovative practices," *Agric. Water Manag.*, vol. 146, pp. 84–94, 2014. https://doi.org/10.1016/j.agwat.2014.07.012

[5] K. Chojnacka, A. Witek-Krowiak, K. Moustakas, D. Skrzypczak, K. Mikula, and M. Loizidou, "A transition from conventional irrigation to fertigation with reclaimed wastewater: Prospects and challenges," *Renew. Sustain. Energy Rev.*, vol. 130, p. 109959, 2020. https://doi.org/10.1016/j.rser.2020.109959

[6] M. A. Zoljalali and E. Omidbakhsh Amiri, "Study of the flow distribution in parallel micro-channels with a triangular manifold," *J. Brazilian Soc. Mech. Sci. Eng.*, vol. 42, no. 1, pp. 1–9, 2020. https://doi.org/10.1007/s40430-019-2140-x

[7] J. P. Hoffstaedt, D. P. K. Truijen, J. Fahlbeck, L. H. A. Gans, M. Qudaih, A. J. Laguna, J. De Kooning, K. Stockman, H. Nilsson, P.-T. Storliet, and et al., "Low-head pumped hydro storage: A review of applicable technologies for design, grid integration, control and modelling," *Renew. Sustain. Energy Rev.*, vol. 158, p. 112119, 2022. https://doi.org/10.1016/j.rser.2022.112119

[8] R. B. Zanca, F. D. G. B. D. Silva, D. O. SantAnna, A. T. Y. L. Silva, H. F. V. Nova, I. F. D. Santos, and J. A. T. D. Reis, "Modeling and hydraulic performance evaluation of a dripper device coupled to a branched water distribution network," *Rev. Ambient. e Agua*, vol. 14, no. 3, pp. 445–458, 2019. https://doi.org/10.4136/ambi-agua.2340

[9] W. A. H. Altowayti, N. Othman, H. A. Tajarudin, A. Al-Dhaqm, S. M. Asharuddin, A. Al-Gheethi, A. F. Alshalif, A. A. Salem, M. F. M. Din, N. Fitriani, and et al., "Evaluating the pressure and loss behavior in water pipes using smart mathematical modelling," *Water*, vol. 13, no. 24, pp. 1–20, 2021. https://doi.org/10.3390/w13243500

[10] P. Yue, H. Yang, C. He, G. M. Yu, J. J. Sheng, Z. L. Guo, C. Q. Guo, and X. F. Chen, "Theoretical approach for the calculation of the pressure drop in a multibranch horizontal well with variable mass transfer," *ACS Omega*, vol. 5, no. 45, pp. 29 209–29 221, 2020. https://doi.org/10.1021/acsomega.0c03971

[11] E. Boyko, H. A. Stone, and I. C. Christov, "Flow rate-pressure drop relation for deformable channels via fluidic and elastic reciprocal theorems," *Phys. Rev. Fluids*, vol. 7, no. 9, p. L092201, 2022. https://doi.org/10.1103/PhysRevFluids.7.L092201

[12] C. R. Camp, E. J. Sadler, and W. J. Busscher, "A comparison of uniformity measures for drip irrigation systems," *Trans. Am. Soc. Agric. Eng.*, vol. 40, no. 4, pp. 1013–1020, 1997. https://doi.org/10.13031/2013.21353

[13] B. Zardin, G. Cillo, C. A. Rinaldini, E. Mattarelli, and M. Borghi, "Pressure losses in hydraulic manifolds," *Energies*, vol. 10, no. 3, p. 310, 2017. https://doi.org/10.3390/en10030310

[14] B. D. Gajbhiye, A. K. Chaturvedi, S. S. Sawant, S. N. Gosavi, H. A. Kulkarni, and C. S. Mathpati, "CFD simulations of flow and pressure drop in T-Junction," in *68th Annual Session of Indian Institute of Chemical Engineers*, 2015.

[15] D. Rehman, D. Barattini, C. Hong, and G. L. Morini, "Effect of aspect ratio and inlet manifold shape on the laminar-to-turbulent transition of gas flow in rectangular microchannels," *Exp. Fluids*, vol. 62, no. 3, p. 52, 2021. https://doi.org/10.1007/s00348-021-03137-3

[16] M. S. Darweesh, W. A. Salah, T. M. Awwad, E. M. Ragab, and A. A. Ahmed, "An improved form of hazen-williams equation for pressurized flow," *Eng. Technol. Appl. Sci. Res.*, vol. 14, no. 3, pp. 14 640–14 644, 2024. https://doi.org/10.48084/etasr.7511

[17] R. Jamil and M. A. Mujeebu, "Empirical relation between Hazen-Williams and Darcy-Weisbach equations for cold and hot water flow in plastic pipes," *Water*, vol. 10, pp. 104–114, 2019. https://doi.org/10.14294/WATER.2019.1

[18] A. Szpicer, W. Bińkowska, I. Wojtasik-Kalinowska, S. M. Salih, and A. Półtorak, "Application of computational fluid dynamics simulations in food industry," *Eur. Food Res. Technol.*, vol. 249, no. 6, pp. 1411–1430, 2023. https://doi.org/10.1007/s00217-023-04231-y

[19] S. Mozaffari, E. Amini, H. Mehdipour, and M. Neshat, "Flow discharge prediction study using a CFD-based numerical model and gene expression programming," *Water*, vol. 14, no. 4, pp. 1–15, 2022. https:

//doi.org/10.3390/w14040650

[20] A. K. Saini, K. Paritosh, A. K. Singh, and V. Vivekanand, "CFD approach for pumped-recirculation mixing strategy in wastewater treatment: Minimizing power consumption, enhancing resource recovery in commercial anaerobic digester," *J. Water Process Eng.*, vol. 40, p. 101777, 2021. https://doi.org/10.1016/j.jwpe.2020.101777

[21] A. Mishra and A. Mukherjee, "A study on energy efficient routing in smart water distribution network using the ACO algorithm," *Uncertain. discourse Appl.*, vol. 1, no. 2, pp. 237–244, 2024.

[22] V. Stepanov, M. Korchagina, S. Kireev, and A. Bill, "Optimization of plunger pump suction manifold parameters," *Transp. Res. Procedia*, vol. 63, pp. 778–788, 2022. https://doi.org/10.1016/j.trpro.2022.06.074

[23] N. Odier, T. Poinsot, F. Duchaine, L. Gicquel, and S. Moreau, "Inlet and outlet characteristics boundary conditions for large eddy simulations of turbomachinery," in *Turbo Expo: Power for Land, Sea, and Air*, 2019, p. V02CT41A020. https://doi.org/10.1115/GT2019-90747

[24] F. Ding, Z. Mao, and K. Han, "Static pressure distribution along the main current channel of drip irrigation pipe," *IOP Conf. Ser. Earth Environ. Sci.*, vol. 199, no. 3, p. 032047, 2018. https://doi.org/10.1088/1755-1315/199/3/032047

[25] E. H. Sharu and M. S. Ab Razak, "Hydraulic performance and modelling of pressurized drip irrigation system," *Water*, vol. 12, no. 8, p. 2295, 2020. https://doi.org/10.3390/W12082295

[26] M. Y. Tayel, A. M. El-Gindy, and H. A. Mansour, "Effect of drip irrigation circuits design and lateral line length on: III-dripper and lateral discharge," *J. Appl. Sci. Res.*, pp. 2725–2731, 2012.

[27] H. Yurdem, V. Demir, and A. Degirmencioglu, "Development of a software to determine the emitter characteristics and the optimum length of new designed drip irrigation laterals," *Math. Comput. Appl.*, vol. 16, no. 3, pp. 728–737, 2011. https://doi.org/10.3390/mca16030728

[28] L. Zhangzhong, P. Yang, S. Ren, Y. Liu, and Y. Li, "Flow characteristics and pressure-compensating mechanism of non-pressure-compensating drip irrigation emitters," *Irrig. Drain.*, vol. 64, no. 5, pp. 637–646, 2015. https://doi.org/10.1002/ird.1929

[29] Y. S. Ong and K. Z. Ku Shaari, "CFD investigation of the effect of manifold and microchannel ratio on the hydrodynamic performance of microchannel heat sink," *SN Appl. Sci.*, vol. 2, no. 7, pp. 1–17, 2020. https://doi.org/10.1007/s42452-020-2990-y

[30] M. K. El-Nemr, "Effect of operating pressure variation on uniformity parameters and its impact on crop productivity and power requirements of trickle irrigation," *Misr J. Agric. Eng.*, vol. 27, no. 4, pp. 1757–1770, 2010. https://doi.org/10.21608/mjae.2010.105343

[31] X. Wang, C. Zhang, and G. Li, "Improving drip irrigation uniformity by boosting the hydraulic performance of drip lateral pressure regulators," *Int. J. Agric. Biol. Eng.*, vol. 17, no. 6, pp. 185–192, 2024. https://doi.org/10.25165/j.ijabe.20241706.8277

[32] A. W. M. Elamin, A. M. Abd Eldaiam, N. A. Abdalla, and M. E. Hussain, "Hydraulic performance of drip irrigation system under different emitter types, and operating pressures using treated wastewater at Khartoum state," *Int. J. Dev. Sustain.*, vol. 6, no. 9, pp. 1086–1095, 2017.

[33] F. Yazici, M. A. Karadag, P. Gokluberk, and A. Kibar, "Examining the uniformity of flow distribution in manifolds," *J. Appl. Fluid Mech.*, vol. 17, no. 5, pp. 989–1001, 2024. https://doi.org/10.47176/jafm.17.05.2302

[34] J. M. Hassan, T. A. Mohamed, W. S. Mohammed, and W. H. Alawee, "Modeling the uniformity of manifold with various configurations," *J. Fluids*, vol. 2014, no. 1, pp. 1–8, 2014. https://doi.org/10.1155/2014/325259

[35] J. Dong, X. Xu, and B. Xu, "CFD analysis of a novel modular manifold with multi-stage channels for uniform air distribution in a fuel cell stack," *Appl. Therm. Eng.*, vol. 124, pp. 286–293, 2017. https://doi.org/10.1016/j.applthermaleng.2017.06.030

[36] H. K. Moffatt, "Helicity and singular structures in fluid dynamics," *Proc. Natl. Acad. Sci. U.S.A.*, vol. 111, no. 10, pp. 3663–3670, 2014. https://doi.org/10.1073/pnas.1400277111

[37] A. Povitsky, "Three-dimensional flow with elevated helicity in driven cavity by parallel walls moving in perpendicular directions," *Phys. Fluids*, vol. 29, no. 8, pp. 1–38, 2017. https://doi.org/10.1063/1.4996179

[38] M. W. Scheeler, D. Kleckner, D. Proment, G. L. Kindlmann, and W. T. M. Irvine, "Helicity conservation by flow across scales in reconnecting vortex links and knots," *Proc. Natl. Acad. Sci. U.S.A.*, vol. 111, no. 43, pp. 15 350–15 355, 2014. https://doi.org/10.1073/pnas.1407232111

[39] R. Perinajová, J. F. Juffermans, J. J. Westenberg, R. L. van der Palen, P. J. van den Boogaard, H. J. Lamb, and S. Kenjereš, "Geometrically induced wall shear stress variability in CFD-MRI coupled simulations of blood flow in the thoracic aortas," *Comput. Biol. Med.*, vol. 133, p. 104385, 2021. https://doi.org/10.1016/j.compbiomed.2021.104385

[40] K. Elonggo, N. A. Nor Salim, and I. Taib, "Computational modelling to predict the pressure loss coefficient of

pipe fitting at KKTDI," *Prog. Aerosp. Aviat. Technol.*, vol. 2, no. 2, pp. 59–68, 2022. https://doi.org/10.30880/paat.2022.02.02.007

[41] A. Kadayifci, G. I. Tuylu, U. Senyigit, and H. Oz, "A research on determining the friction losses formed in the small diameter floppy polythene pipe lines," *African J. Biotechnol.*, vol. 9, no. 3, pp. 307–313, 2010.

[42] M. Tayel, D. Lightfoot, and H. Mansour, "Effect of drip irrigation circuits design and lateral line length on: II-flow velocity and velocity head," *Agric. Sci.*, vol. 3, no. 4, pp. 531–537, 2012. https://doi.org/10.4236/as.2012.34063